

Breaking the 49-Qubit Barrier in the Simulation of Quantum Circuits

Edwin Pednault^{*1}, John A. Gunnels^{†1}, Giacomo Nannicini^{†1}, Lior Horesh¹, Thomas Magerlein², Edgar Solomonik³, Erik W. Draeger⁴, Eric T. Holland⁴, and Robert Wisnieff¹

¹IBM T.J. Watson Research Center, Yorktown Heights, NY

²Tufts University, Medford, MA

³Dept. of Computer Science, University of Illinois at Urbana-Champaign, Champaign, IL

⁴Lawrence Livermore National Laboratory, Livermore, CA

Abstract

With the current rate of progress in quantum computing technologies, systems with more than 50 qubits will soon become reality. Computing ideal quantum state amplitudes for devices of such and larger sizes is a fundamental step to assess their fidelity, but memory requirements for such calculations on classical computers grow exponentially. In this study, we present a new approach for this task that extends the boundaries of what can be computed on a classical system. We present results obtained from a calculation of the complete set of output amplitudes of a universal random circuit with depth 27 in a 2D lattice of 7×7 qubits, and an arbitrarily selected slice of 2^{37} amplitudes of a universal random circuit with depth 23 in a 2D lattice of 8×7 qubits. Combining our methodology with other decomposition techniques found in the literature, we show that we can simulate 7×7 -qubit random circuits to arbitrary depth by leveraging secondary storage. These calculations were thought to be impossible due to memory requirements; our methodology requires memory within the limits of existing classical computers.

1 Overview of the paper

In the last few years, significant technological progress has enabled quantum computing to evolve from a visionary idea [14] to reality [8, 9]. With existing devices now providing 20–50 qubits with controllable couplings, the topic of “quantum supremacy” — that is, the ability of a quantum device to perform a computational task beyond what any classical computer can perform — is receiving much attention [20, 29, 5, 1, 13]. Among the many issues faced in advancing quantum computing technology, two are particularly relevant for this paper: (1) the ability to quantify circuit fidelity (e.g., [4, 30, 16, 5, 24]), and (2) the ability to assess correctness, performance and scaling behavior of quantum algorithms [17]. Fundamental to both is the ability to calculate quantum state amplitudes for measured outcomes — a task whose difficulty grows exponentially in the size of the circuit. This paper presents a new methodology for this task that can handle circuits of much larger size than that previously found in the literature. Our approach to calculating quantum amplitudes uses a tensor representation [21], combining the flexibility of tensor computations with tensor slicing methods, to enable final quantum states of circuits to be calculated in slices instead of having to materialize entire quantum states in memory.

^{*}Corresponding author; pednault@us.ibm.com

[†]These authors contributed equally.

We apply our methodology to *universal random circuits* constructed according to the rules described in [5]. These circuits can be embedded in a 2D lattice of qubits with nearest-neighbor couplings. The depth of such a circuit is the number of layers that the circuit can be partitioned into, in such a way that at any given layer at most one gate acts on a qubit. As in [5], we do not count the first layer of Hadamard gates in the depth.

We simulate two quantum circuits: one with depth 27 for a 7×7 grid of qubits, the other with depth 23 for an 8×7 grid of qubits. The primary data structures employed in the depth-27 simulation require just over 4.5 Terabytes of main memory to store results, and just over 3.0 Terabytes for the depth-23 simulation. In contrast, existing state-of-the-art techniques [19] would have required 8 Petabytes and 1 Exabyte, respectively. More recent work [6, 5, 23, 11, 10], that followed a preprint of this paper, has simulated larger circuits using similar techniques. We also present extensions of our simulation technique to combine it with the decomposition approaches discussed in [1, 19]. The goal of these extensions is the simulation of quantum circuits with larger depth than discussed above. We show that single amplitudes of a 7×7 , depth 46 circuit can in principle be computed on the supercomputer used in our tests in just a few hours using 141 TB of memory, and we propose a simulation strategy that is able to simulate such a circuit to arbitrary depth in reasonable time (e.g., less than a day for a depth-83 circuit) by leveraging secondary storage. We do not test these extensions computationally, but we describe the foundations of the methodology and estimate the computational effort that these experiments would require. The simulation of 7×7 circuits to arbitrary depth was thought to be out of reach [5, 23, 10].

The simulation of the 7×7 , depth 27 and 8×7 , depth 23 circuits was performed at Lawrence Livermore National Laboratory on the Vulcan supercomputer, an IBM Blue Gene/Q system. We used the simulation on Vulcan to investigate the isotropic properties of the resulting distributions of quantum-state probabilities. Theory predicts that these probabilities should exhibit exponential (a.k.a. Porter-Thomas [28]) distributions across the aggregate quantum state [5]. However, because the pattern in which these probabilities occur within the final quantum state is also chaotic, the same exponential distribution of probabilities should be observed within small local slices of the state as well. Our simulations confirm this phenomenon.

2 Simulation methodology: preliminaries

The majority of this paper is devoted to a high-level description of the simulation methodology introduced in this paper; further details and an in-depth literature review are provided in the Appendix. The input of a simulation algorithm is a description of a quantum circuit, and a specification of a set of amplitudes (i.e., coefficients of the quantum state obtained at the end of the circuit) that have to be computed; we are mainly interested in the case in which all amplitudes have to be computed, but we will study the case of single amplitude calculations as well.

Our analysis considers a hierarchy of storage devices, which has two levels in its simplest form: primary storage, i.e., RAM, and secondary storage, i.e., disk. Descending the hierarchy increases available space but decreases access speed: the performance of a simulation strategy should take into account space occupancy and number of accesses at all levels of the hierarchy. This distinction is crucial from a practical point of view. For example, the full quantum state of a 49-qubit system requires 2^{49} complex numbers (8 PB in double precision); this eliminates the possibility of keeping the entire state in primary storage, but does not rule this out for secondary storage. Thus, disk usage must be allowed in order to have enough space to store the simulation output for circuits of this or larger size. The main numerical experiments discussed in this paper employ main memory only to store intermediate results, but the Appendix describes how disk can be used to simulate a 7×7 -qubit circuit to arbitrary depth. Of course, a single amplitude can in principle be computed using linear space and exponential time (i.e., number of floating point operations), using the Feynman path approach, see e.g., [6]. However, the



Figure 1: Example of a tensor network for the expression $\sum_j A_i^j v_j$.

time requirement of such an approach grows intractable very quickly with increasing circuit size. We desire simulation algorithms with manageable time requirements (i.e., hours – not days), which from a practical standpoint implies a small number of floating point operations per amplitude per gate.

In very broad terms, our approach consists of partitioning a quantum circuit into subcircuits that can be simulated independently and then recombined to obtain the desired result. Of course, a quantum circuit cannot in general be split into subcircuits to be simulated independently due to entanglement. However, when the action of the circuit is represented in a purely algebraic manner, e.g., using a graphical model known as a tensor network [21, 25], it can be verified that arbitrary splitting into subcircuits can be performed, although it may require additional memory to account for entanglement between subcircuits. As a consequence, not all decompositions of a circuit into subcircuits are memory-efficient.

A description of our simulation algorithm requires some preliminary discussion regarding tensor networks. A *tensor* is a multilinear map (i.e., a multidimensional generalization of a matrix), equipped with a set of indices to address its elements; each index varies within a specified range, which we always assume to be the set $\{0, 1\}$ in this paper — corresponding to the basis elements $|0\rangle, |1\rangle$ for the vector space \mathbb{C}^2 in which the state of a single qubit lives. The number of indices of a tensor is called its *rank*. It follows that a rank- k tensor requires $O(2^k)$ storage in general. A *tensor network* is a graph $G = (V, E)$ in which each node is associated with a tensor and each edge with an index of the adjacent tensor(s). Edges between nodes represent shared indices that must be summed over. For example, one possible way to represent a matrix-vector multiplication in a tensor network is shown in Fig. 1. The edge j between the tensors A_i^j and v_j represents the operation $\sum_j A_i^j v_j$. A summation over shared indices is called a *contraction*. Given a tensor, it is natural to distinguish between input indices, associated with a dual space (e.g., the rows of a matrix), and output indices, associated with a primal space (e.g., the columns of a matrix). For example, A_i^j is a tensor with one input index i and one output index j .

The tensor network associated with a quantum circuit contains a tensor for each gate, a tensor for the initial state of each qubit, and a tensor for the output state under consideration on those qubit lines for which the outcome $\langle 0 |$ or $\langle 1 |$ has been specified. Edges follow the qubit lines. In this paper we consider only single and two-qubit gates, without loss of generality since any quantum gate can be approximated to arbitrary precision using only single and two-qubit gates. A single-qubit gate is represented as a rank-2 tensor (one edge entering, one edge leaving the associated node), corresponding to a 2×2 matrix, and a two-qubit gate is represented as a rank-4 tensor (two edges entering, two edges leaving), corresponding to a 4×4 matrix.

State-of-the-art methodologies for quantum circuit simulation are for the most part based on the tensor network representation of the circuit discussed as described above, which we will refer to as *circuit graph*. A seminal work in the area is [25], describing a simulation algorithm that runs in time exponential in the treewidth of the line graph of the circuit graph (the treewidth of the line graph is within a constant factor of the treewidth of the circuit graph). Numerical experiments with this methodology are presented in [15]. After a preprint of our paper was posted online (i.e., version 1 of this arXiv paper), a series of recent works [6, 23, 11, 10] have tackled the problem with related techniques, increasing the size or depth of circuits that can be simulated. The best known upper bounds on the computational complexity of simulating quantum circuits of the class studied in this paper are given in [1]. The Appendix discusses the existing literature in more detail.

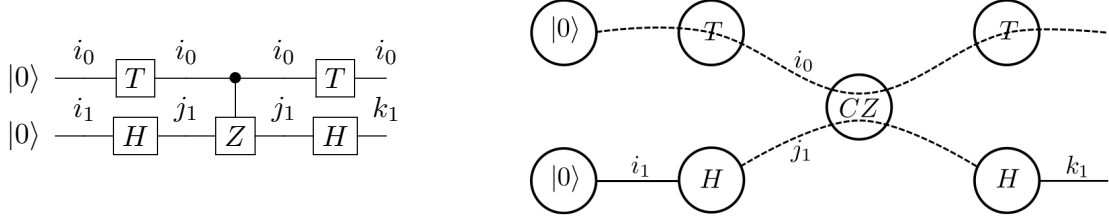


Figure 2: Example of the proposed tensor network representation of a quantum circuit (left), using a hypergraph (right). The T and CZ gates are diagonal. Dashed edges are hyperedges, solid edges are “regular” edges, i.e., hyperedges of cardinality two.

3 Simulation methodology: main building blocks

We propose an approach that builds on the foundations of tensor networks, with some generalizations to allow for more flexibility in the calculations, especially when we are interested in computing the entire state vector rather than single amplitudes. Three ideas are crucial for our approach: using hyperedges to exploit diagonal gates, allowing contractions between non-adjacent nodes of the tensor network, and slicing. The first two ideas are not discussed in the literature on tensor networks for quantum circuit simulation, to the best of our knowledge; slicing is used in [19]. We describe these ideas below.

Formally, we call a gate *diagonal* if the associated tensor $A_{i_1, \dots, i_m}^{j_1, \dots, j_m}$ is nonzero only if $i_k = j_k$ for $k = 1, \dots, m$. For example, the 2×2 identity matrix is a diagonal gate; this is a generalization of the concept of diagonal matrices, translated to tensors. For a diagonal gate, because all elements outside the diagonal are zero, it is convenient to assign the same index label to input and output edges, writing the tensor as $A_{i_1, \dots, i_m}^{i_1, \dots, i_m}$. This representation is not only natural, but also more economical in that it reduces the total number of index labels. We remark that in case of a sequence of diagonal gates, the same index label could be associated with multiple edges spanning across multiple nodes of the tensor network. Thus, rather than representing the tensor network as a graph, we use a directed *hypergraph*, in which each hyperedge consists of an ordered sequence of nodes and is associated with a single index label. A hyperedge consisting of just two nodes is equivalent to an edge in the original tensor network. We give an example of this representation in Fig. 2.

This representation of the tensor network as a hypergraph allows us to compute tensor ranks that more accurately correspond to the real memory occupancy in a computer implementation of the simulation algorithm. Indeed, a rank- k diagonal tensor requires only $O(2^{k/2})$ memory, as compared to $O(2^k)$ for non-diagonal tensors; consequently, it is incident to $k/2$ hyperedges. This type of consideration plays a crucial role when determining how to partition a tensor network into manageable subgraphs (corresponding to subcircuits). The savings become clear in constructing the line graph of the proposed hypergraph: the line graph of a diagonal two-qubit gate (e.g., controlled-Z gate) is a 4-clique in the traditional tensor network representation, but is only a 2-clique in the proposed representation. This contributes to reducing the treewidth; more details are given in the Appendix.

The second idea that is crucial for our method is the contraction of non-adjacent nodes in the hypergraph. As mentioned earlier, existing simulation methodologies based on tensor networks rely on determining a sequence of contractions between adjacent vertices that leads to the contraction of the entire graph to a single node [25, 6]. In our setting, this is not a viable approach. Since we are interested in determining the whole state vector for an n -qubit system, rather than a single amplitude, a straightforward application of a sequential tensor contraction method would lead to tensors of size proportional to 2^n simply due to the number of open ranks; i.e., the edges at the end of the circuit that are not connected to an output state $\langle 0 |$ or $\langle 1 |$. We instead allow contraction of arbitrary sets of nodes in the hypergraph. Such a contraction performs the usual summation over shared indices (i.e., edges interior to the set being

contracted), and applies an outer product to the non-shared indices. This approach allows us to retain flexibility in the order in which contractions are performed to reduce memory requirements.

In broad terms, we partition the tensor network into sub-hypergraphs corresponding to subcircuits, each of which includes fewer qubits than the initial circuit. Within each subcircuit, we perform computations following Schrödinger’s approach; that is, starting from the initial state (i.e., the generalized contraction of the tensor $|0\rangle$ for the qubits under consideration, corresponding to an outer product), we apply layers of quantum gates one at a time. If there are any two-qubit gates connecting two different subcircuits, we defer their application and do not perform the corresponding (adjacent) contraction until the subsequent stage of the computation. This deferral leaves open ranks in the corresponding tensors, increasing memory consumption, but avoids merging potentially large subcircuits. Eventually the subcircuits have to be merged to compute the final quantum state, or to initialize the state of a subsequent tensor in the circuit.

The third and final building block of our methodology is slicing. The idea is to select certain hyperedges in the hypergraph, say s of them, loop over the 2^s possible combinations of values for these hyperedges, and perform the remaining computations with the value for these hyperedges fixed. This yields 2^s “sliced” tensors. If the choice is made appropriately, the resource consumption of each sliced tensors is a factor 2^s smaller than the whole circuit. Since there are 2^s sliced tensors, it may seem that this does not yield any savings; however, our approach tries to reorder the tensor computations so that only a few selected slices (rather than the full tensor) need reside in primary storage, thus decreasing resource consumption and better exploiting parallelism.

In the Appendix, we formalize our methodology and illustrate how these three ideas can be applied on a small example circuit. In general, due to the large number of possible circuit decompositions, several considerations need to be taken into account to determine an appropriate simulation strategy. This will be discussed next.

4 Optimizing the circuit simulation strategy

For a given input quantum circuit, there is an exponentially large number of possible circuit partitionings and sequencings of the computations. Additionally, for every CX gate we have the choice of keeping it as is, or transforming it into two Hadamard gates and one CZ gate, which may be beneficial because CZ is a diagonal gate. These options generate a space of possible computation schemes for any given circuit. Given a circuit and a computation scheme, we can compute the memory and floating-point operations required simply by analyzing subcircuits. In principle, we would like to run a multi-objective optimization over the space of possible computation schemes to generate the Pareto frontier that defines the optimal trade-off between memory usage and floating-point operations. However, a brute force exploration strategy of all combinations is not viable for circuits above a modest size.

To obtain the numerical results presented in this paper, we employed two heuristic search strategies: one that implemented some hand-crafted circuit partitioning criteria based on our intuitions, and one that explored the choices described above in a largely depth-first manner. The hand-crafted strategies adopted the following principles:

- Diagonalize CX gates if all subsequent gates applied to the control qubit are diagonal or diagonalizable.
- Try to keep each circuit partitioned into a small number of (e.g., less than five) subcircuits, with a small number of gates crossing the boundaries.

The Appendix illustrates how the 49-qubit, depth 27 random circuit and the 56-qubit, depth 23 random circuit used in our numerical study were partitioned into subcircuits using the hand-crafted approach described above.

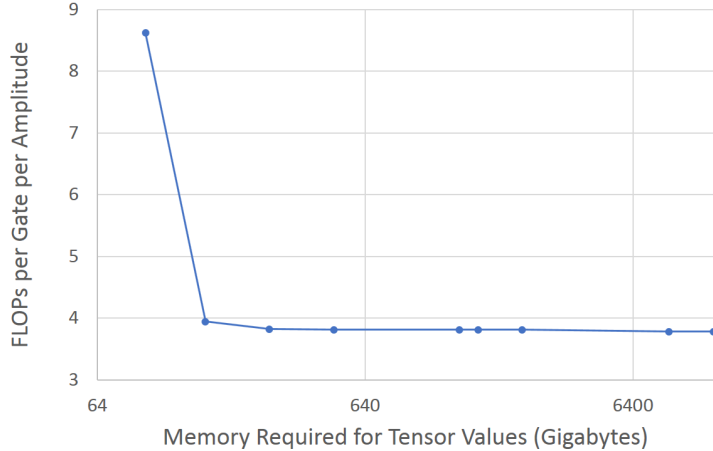


Figure 3: Trade-off between floating point operations and memory usage.

We used the largely depth-first heuristic search to explore the trade-off between memory usage and floating-point operations for various circuits. In each execution, the search method was given a circuit and a limit on the available memory that could be used, and it then attempted to find circuit partitionings that minimized the number of floating-point operations needed to perform a simulation without exceeding the specified primary memory limit. Fig. 3 illustrates the trade-off between memory and computation identified by the analysis for the 49-qubit circuit used in our numerical study. Since the search strategy employed was given a time limit, it is likely that this curve is suboptimal and circuit partitioning schemes that strictly dominate ours could be found.

5 Software and hardware platform

We implemented the quantum circuit simulation approach described above using the Cyclops Tensor Framework (CTF) [32], a distributed-memory C++ library for tensor summations and contractions. The library provides a domain-specific language for tensor operations using an Einstein-summation syntax. CTF tensors are distributed over all processors with tensor summations and contractions performed in a data-parallel manner using MPI [18], OpenMP [12], and BLAS [22].

The massively parallel tensor contraction calculations enabled by CTF have heretofore been driven by applications in computational chemistry and physics [2, 27] that involve contractions of tensors with 4 to 8 dimensions; the quantum circuit models employed in our calculation use tensors of much higher dimensionality. In performing these contractions using CTF, the main challenge is the need for higher-dimensional virtual topologies (i.e., the decomposition of tensors among more dimensions) than CTF typically performs. CTF operates by mapping tensor dimensions onto dimensions of a processor grid, often redistributing tensors to new mappings at contraction time. As all the dimensions of our tensors are small, mappings to high-dimensional processor grids are necessary. To achieve these, we increased the space of virtual topologies CTF considers, made improvements to the mapping logic in CTF, and enabled dynamic creation and destruction of MPI communicators (defined for each processor grid dimension).

We used the built-in profiling capabilities of CTF and the performance-counter libraries made available on the hardware platform used in our experiments to determine the bottlenecks within CTF incurred during circuit simulation contractions [26]. For reasons of brevity, we do not describe all optimizations in this paper. Local copy, summation, and multiplication primitives were automatically replaced by appropriate optimized variants, chosen with knowledge of the parameters employed during the circuit simulations. These low-level changes substantially improved the performance with respect to the origi-

nal implementation.

Our experiments were executed on Vulcan, a 24,576-node IBM Blue Gene/Q supercomputer [33]. A Blue Gene/Q node consists of 18 A2 PowerPC 64 bit cores, 16 of which are application-accessible. Each A2 core runs at 1.6 GHz, has a 16 KB private level 1 (L1) cache, as well as a 2 KB prefetching buffer (L1P). All the cores on the same processor share a 32 MB level 2 (L2) cache and 16GB of main memory. The compute nodes are connected via a 5D torus network with a total network bandwidth of 40 GB/s.

6 Numerical results

We now present the results of our experiments. In the case of the 49-qubit circuit, the final quantum state was calculated in 2^{11} slices with 2^{38} amplitudes each. In the case of the 56-qubit circuit, only one slice with 2^{37} amplitudes was calculated out of the 2^{19} such slices defining the final quantum state.

All experimental results were obtained over the course of two days. This time included the time to setup the experiments described in this paper, as well as that to conduct additional experiments beyond the scope of what is described here.

Memory usage required scaling to 4,096 nodes, with 64 TB of memory, for each (parallel) calculation. The theoretical minimum memory footprint to hold a slice of the state vector is less than 5 TB for the 49-qubit circuit (2^{38} complex doubles are used to store the 2^{38} amplitudes); it is common in the literature to report just the memory required for the state vector, e.g., [19]. In practice, experiments required more than 32 TB. The bulk of these operations require two large tensors to compute a result and CTF internal buffering introduces approximately a factor of 4 in overhead. Memory was also needed to reformat contraction operands for efficiency and for buffer space as messages are passed between nodes.

After computing the ideal state amplitudes, we analyzed the distributions of the corresponding outcome probabilities (i.e., the squared magnitudes of the amplitudes) in aggregate across slices as well as individually per slice. The ranges of these outcome probabilities vary with the number of possible outcomes $N = 2^n$, where n is the number of qubits. The values of these probabilities also vary over several orders of magnitude. For these reasons, histograms were calculated for the values of $z = \log(Np)$ for outcome probabilities p . This transformation normalizes the resulting histograms across varying numbers of qubits, simplifying their comparison. It also better reveals the full dynamic range of the outcome probabilities. The theoretical probability density of $z = \log(Np)$ for universal random circuits with circuit fidelity α is distributed according to the following equation (see the Appendix for its derivation), which describes a truncated Gumbel distribution in the case of a perfect fidelity of $\alpha = 1$:

$$f_z(z) = \frac{d}{dz} F_z(z) = \begin{cases} \frac{\frac{1}{\alpha} e^z - \frac{1}{\alpha} (e^z + \alpha - 1)}{1 - e^{-N}} & 1 - \alpha \leq e^z \leq 1 + (N - 1)\alpha \\ 0 & \text{otherwise.} \end{cases} \quad (1)$$

Fig. 4 shows the histograms of the log-transformed outcome probabilities, $\log(Np)$, obtained for the 49- and 56-qubit circuits plotted together with their theoretical distributions given by Equation (1) for $\alpha = 1$. The histogram for the 49-qubit circuit incorporates all 2^{49} outcome probabilities, while the one for the 56-qubit circuit incorporates only the arbitrarily selected slice of 2^{37} outcome probabilities that were calculated for that circuit. As these graphs illustrate, there is an extremely close agreement between the observed and predicted distributions in both cases.

Fig. 5 shows a plot of the histograms obtained for an aggregation of the slices calculated for the 49-qubit circuit. Each histogram is an aggregation of 32 slices, and the 64 individual histograms have been stacked together and rendered as a surface plot to better reveal variations between the histograms. As can be seen in this figure, the variations are concentrated at the extreme tail ends of the distribution where very low probabilities and, hence, very low bin counts are observed in the histograms. Such

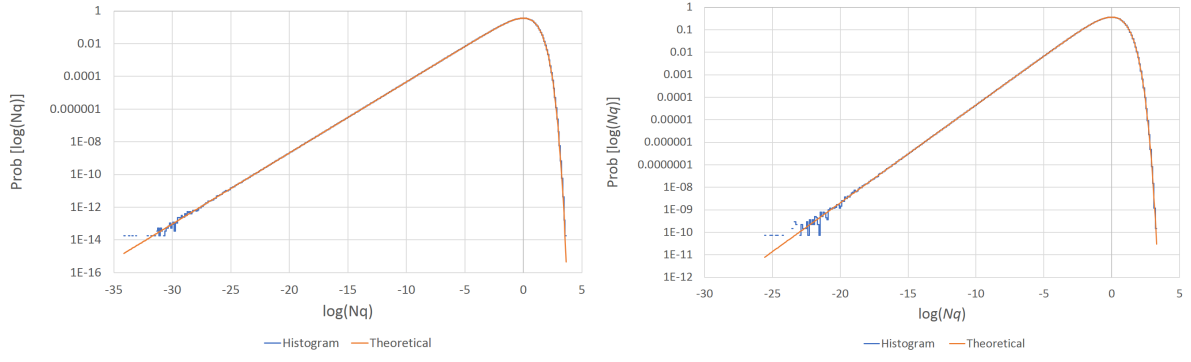


Figure 4: Histograms of log-transformed outcome probabilities calculated for the 49-qubit circuit (left) and the 56-qubit circuit (right), compared to their theoretically predicted distributions.

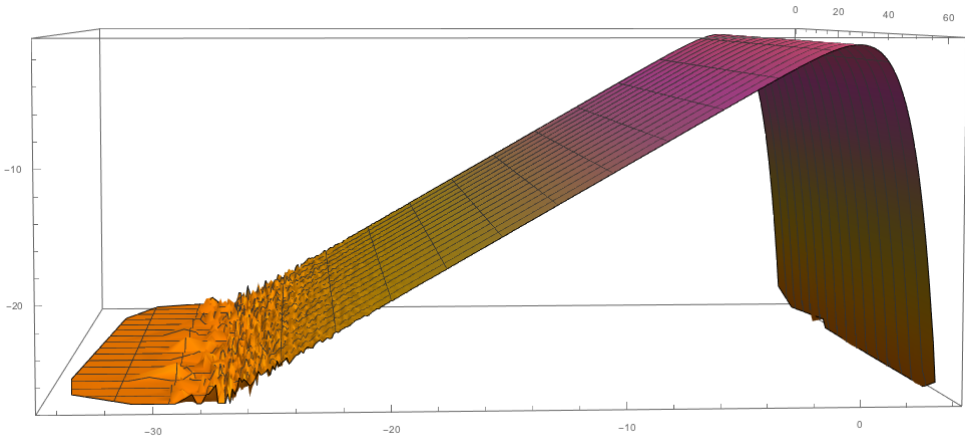


Figure 5: Histograms of log-transformed outcome probabilities for the individual slices of the 49-qubit circuit rendered together as a surface plot. The vertical axis is plotted on a log-scale for consistency with Fig. 4.

variations are expected in histograms whenever one is dealing with low bin counts. The visual effects are magnified in this case because the vertical axis (corresponding to bin counts) is plotted on a log scale. The same magnification effect can be observed in Fig. 4. Except for such minor variations at low bin counts, Fig. 5 reveals that the distributions of outcome probabilities across slices are virtually identical, demonstrating that this distribution is essentially isotropic across the quantum state.

In the Appendix, we discuss further quantum circuit simulations enabled by the ideas presented in this paper that involve circuits with more layers of gates. While we did not carry out these simulations, our framework allows us to verify that the memory and floating point operation requirements for these computations are viable on Vulcan or similar supercomputers. More specifically, we show that the computation of single amplitudes, rather than the full state vector, for a 7×7 universal random circuit of depth 46 can be performed on Vulcan in a matter of a few hours. Furthermore, combining targeted slicing with sporadic disk read/write operations, as already suggested by [19], we provide an algorithm to simulate a 7×7 universal random circuit up to arbitrary depth, outputting all amplitudes to disk. Safe estimates summarized in Table 1 show that for a depth-83 circuit, this experiment could take ≈ 3.5 days on Vulcan, but would be completed in less than a day on Sequoia, the larger Blue Gene/Q supercomputer at Lawrence Livermore National Laboratory, and on Summit, the IBM-Power9/NVIDIA-

Storage System	Size (PB)	Depth 55 Single Precision (hours)	Depth 55 Double Precision (hours)	Depth 83 Single Precision (hours)	Depth 83 Double Precision (hours)
Summit Burst Buffer	7	7.16		11.58	
Summit File System	250	7.97	9.00	13.19	15.26
Sequoia File System	50	9.68	12.42	16.60	22.09
Vulcan File System	5	48.92		86.85	

Table 1: Estimates of total run times, including secondary storage read/write times of various precisions, for the computation of full quantum state vectors of deep 7×7 -qubit circuits.

Volta supercomputer currently being installed at the Oak Ridge National Laboratory.

7 Conclusions

The key contribution of our paper is a new circuit simulation methodology that allowed us to break the 49-qubit barrier, previously thought to be the limit beyond which quantum computers cannot be simulated. Our results confirm the expected Porter-Thomas distribution as the distribution of the outcome probabilities for universal random circuits.

The trade-off between memory and time requirements depicted in Fig. 3 shows that the boundary for classical simulation of universal random circuits stretches beyond 49 qubits. In the case of 49-qubit circuits, we show that we can reach a depth of 46 for the computation of single amplitudes using only primary storage, and arbitrary depth for the computation of all amplitudes by leveraging secondary storage. In the latter case, the total time is still dominated by computation and communication time, rather than disk read/write operations.

Our simulations demonstrate that the computation of quantum amplitudes for measured outcomes for quantum devices of approximately 50 qubits is possible with existing classical computing resources. The exponential growth of the necessary computational resources implies that classical computers will eventually not be able to simulate the behavior of emerging universal quantum computers; however, for the class of quantum circuits studied in this work, we are not at that stage yet.

Acknowledgments

We are very grateful to Jonathan L. DuBois, Jay Gambetta, Ramis Movassagh, John Smolin, Fred Streitz, Maika Takita, Robert Walkup, and Chris Wood. Work of Tom Magerlein was performed during an internship at the IBM T.J. Watson Research Center. Work of Erik W. Draeger and Eric T. Holland was performed under the auspices of the U.S. Department of Energy by the Lawrence Livermore National Laboratory under Contract No. DE-AC52-07NA27344. This work was supported in part by the Laboratory Directed Research and Development under Grant No. 16-SI-004.

A Appendix

The majority of this appendix is devoted to a detailed explanation of the mathematical foundations of our quantum circuit simulation methodology. Some of the concepts are repeated from the main text, but here we provide a more formal exposition that is useful to give a precise description of the algorithms. Based on these foundations, we describe a methodology to simulate deep 49-qubit circuits, up to arbitrary depth, giving a safe estimate of the required wall-clock time to show feasibility of such simulations. Finally, we discuss the relationship between our hypergraph representation with that of [25, 6], and we provide the derivation of the distribution of $\log(Np)$ (where p is the outcome probability and $N = 2^n$ the size of the Hilbert space) used in the main text.

A.1 Preliminaries

The description of diagonal tensors in the main text of the paper emphasizes that input index labels can carry over to output index labels, which may lead to the same index label appearing multiple times when there is a connected sequence of diagonal gates. We therefore define a *tensor network* as a hypergraph $G = (V, E, \lambda)$ consisting of:

- A vertex set V , such that each tensor is associated with a vertex.
- A hyperedge multiset E , such that each hyperedge e is an ordered subset of 2^V .
- A labeling function λ that associates a unique index label with each hyperedge $e \in E$.

For every hyperedge $e \in E$, we call *tail* the first node of e , *head* the last node of e .

The literature contains some examples of this type of tensor networks, see e.g., [7, 31], but to the best of our knowledge these concepts were not formalized and systematically used in the context of quantum circuit simulation.

Contractions can be defined on the type of tensor network indicated above. Since, as discussed in the main text, our simulation algorithm also employs contractions between non-adjacent nodes, which are not standard in the tensor network literature, we give our own definition of contraction. Given a tensor network $G = (V, E, \lambda)$ and two vertices $u, v \in V$, we define a *contraction* of u, v as the tensor network $G' = (V', E', \lambda')$ such that:

- (a) $V' = V \setminus \{u, v\} \cup \{w\}$.
- (b) E' is obtained from E by replacing, for each hyperedge, each maximal occurrence of a subsequence containing only u and v with w . The label $\lambda(e')$ for a contracted hyperedge e' is the same as the label $\lambda(e)$ for the original hyperedge e .
- (c) The tensor T associated with w is obtained as follows. Let A be the tensor associated with u , B the tensor associated with v . Let S_{uv} be the set of index labels associated with hyperedges of the form $\{u, v\}$, S_{vu} the set of index labels associated with hyperedges of the form $\{v, u\}$. Let I_A (resp. I_B) be the set of all input index labels for A (resp. B), O_A (resp. O_B) be the set of all output index labels for A (resp. B). Thus, the tensors A, B can be written as:

$$A^{\{k\}_{k \in S_{uv}} \{\ell\}_{\ell \in O_A \setminus S_{uv}}} \quad B^{\{i\}_{i \in S_{vu}} \{n\}_{n \in O_B \setminus S_{vu}}}.$$

The tensor T is then defined as:

$$T^{\{\ell\}_{\ell \in O_A \setminus S_{uv}} \{n\}_{n \in O_B \setminus S_{vu}}} := \sum_{\{i\}_{i \in S_{vu}}} \sum_{\{k\}_{k \in S_{uv}}} A^{\{k\}_{k \in S_{uv}} \{\ell\}_{\ell \in O_A \setminus S_{uv}}} B^{\{i\}_{i \in S_{vu}} \{n\}_{n \in O_B \setminus S_{vu}}}. \quad (2)$$

We highlight some special cases of the above definition. ‘‘Traditional’’ tensor network contractions occur when the edges $\{u, v\}$ or $\{v, u\}$ exist. In case $S_{uv} = S_{vu} = \emptyset$, the tensor contraction is an outer product between A and B . If A and B are diagonal, T is diagonal.

It is straightforward to note that given any set of nodes, any sequence of pairwise contractions that contracts the entire set yields the same outcome, regardless of the order (although the computational cost of the contraction may depend on such order). Thus, the concept of contraction generalizes naturally to sets of vertices: given a tensor network $G = (V, E, \lambda)$ and a subset of nodes $C \subseteq V$, a contraction of C is a tensor network $G' = (V', E', \lambda')$ obtained by performing pairwise contractions of nodes in C , in any order, until C collapses to a single node.

A.2 Simulation of quantum circuits

A *quantum circuit* on q qubits with depth D is a tensor network with the following properties:

- There are q rank-1 nodes associated with the tensor $|0\rangle$, called the ‘‘initial state’’.
- There are q hyperedges whose head is a rank-1 node associated with the tensor $\langle 0|$, or a rank-1 node associated with the tensor $\langle 1|$, or a special node ‘‘O’’ that is not associated with any tensor and cannot be contracted, representing ‘‘open wires’’. The heads of these q hyperedges are called the ‘‘output state’’.
- Every node in the graph that is not an initial or output state is such that its input rank is equal to the output rank.
- All hyperedges are directed away from the initial state and toward the output state, i.e., there is a topological ordering of the graph such that the initial state precedes every other node, and the output state follows every other node.
- The maximum number of nodes on any path from the initial state to the output state is $D + 2$.

It follows from this definition that the graph can be partitioned into $D + 2$ sets of nodes (‘‘layers’’) with the property that each layer has at most q input hyperedges and q output hyperedges (the ‘‘qubit lines’’). While we assume that every non-boundary tensor in a quantum circuit is either a rank-2 tensor (single-qubit gate) or a rank-4 tensor (two-qubit gate), most of our analysis directly applies to quantum circuits with gates that involve more than two qubits.

Given a quantum circuit $G = (V, E, \lambda)$ on q qubits, a *simulation strategy* for G is a sequence of contractions on G that contracts every node except the special node ‘‘O’’.

We now come to defining the computational requirements for contractions, in terms of memory occupation and number of operations. We are interested in giving upper bounds to such costs. For this, we have to start mixing purely theoretical considerations with practical considerations. We assume that we have access to both primary and secondary storage: primary storage is a fast but more scarcely available resource, e.g., RAM, while secondary storage is slower but available in larger capacities, e.g., disk.

Assume we are given a quantum circuit $G = (V, E, \lambda)$ and a set of nodes $C \subseteq V$ to contract that would result in a rank n tensor. Assume further that there are m hyperedges that are fully contained in C . The result of the contraction takes space $O(2^n)$, and this is a space requirement that cannot be avoided. However, if such a contraction is the final goal of the computation, then the result of the contraction can be stored to disk rather than kept in RAM. Given these considerations, the *computational cost* of a simulation strategy is given by the number of floating point operations to perform the simulation. Its *memory cost* is the amount of space in primary and secondary storage that is required to store all intermediate tensors, i.e., all tensors except the final tensor connected to the special node ‘‘O’’.

A.3 Review of the quantum circuit simulation literature

There are two very well-known ways to perform simulation of a circuit with q qubits and depth D , with different computational cost. The discussion in this section is mainly concerned with asymptotic performance and therefore considers primary storage only.

The first approach, sometimes called the “Schrödinger approach”, consists of contracting the circuit in layers. Given the topological ordering of the circuit, we can partition the circuit into $D + 2$ sets V_0, \dots, V_{D+1} such that V_0 contains the initial state, V_{D+1} the output state, and there is no hyperedge fully contained in each V_d . We first contract V_0 , which creates a $O(2^q)$ -size tensor, and then iteratively contract the newly created node with V_d , one node at a time, for $d = 1, \dots, D + 1$. Since there are no interior hyperedges for any of the sets V_d , every contraction has memory and computational cost $O(2^q)$, for a total of $O(D2^q)$ flops and $O(2^q)$ memory.

The second approach, sometimes called the “Feynman approach”, consists in contracting the entire network in one step. Assume that there are n open output wires, i.e., hyperedges whose head is “O”. Since the number of hyperedges in the circuit is $O(qD)$, the total computational cost is $O(2^{n+qD})$, whereas memory occupation is $O(nD)$.

Recent work in the area provides better upper bounds. [25] shows that the simulation of quantum circuits can be performed in time exponential in the treewidth of the underlying tensor network representation. The setting of [25] assumes that there is a full set of q output states $\langle 0 |$ or $\langle 1 |$, i.e., we are interested in computing only one of the state amplitudes at the end of the circuit. In this setting, simulating a circuit amounts to contracting the entire tensor network to a single node, obtaining a scalar. [25] propose a simulation strategy that always contracts adjacent nodes, according to an order obtained via a tree decomposition of the line graph of the tensor network. This yields a simulation strategy with cost (both computational and memory) exponential in the treewidth of said graph, which is within a multiplicative factor of the treewidth of the tensor network. For a discussion of treewidth and tree decompositions in combinatorial optimization, see [3].

[1] introduces a simulation strategy that yields the best known upper bounds to date. For a general circuit, by recursively splitting the circuit in half according to the layers (i.e., creating two circuits of depth $D/2$, then four circuits of depth $D/4$, and so on), [1] gives an algorithm that takes $O(q(2D)^{q+1})$ time and $O(q \log D)$ memory. Specializing the algorithm to quantum circuits with an underlying two-dimensional grid connectivity graph, the running time decreases to $O(2^n \left[1 + \left(\frac{D}{c\sqrt{q}} \right)^{q+1} \right])$ and space requirement increases to $O(Dq \log q)$. To accomplish this goal, [1] first recursively partitions each layer of the circuit, according to its grid structure, in smaller grids with few edges across the sets of the partition, called a cut set. Because of the grid structure, the number of edges in the cut set is $O(\sqrt{q})$. Then, each set of the partition is equivalent to a depth D circuit with a small number of qubits, and these subcircuits can be contracted independently, provided we allow for extra ranks in the tensors to account for the cut set, and for the computational cost of the final contraction of edges in the cutset. Rather than performing a full contraction of the subcircuits in one step, [1] recursively splits the circuit in half according to the layers, as mentioned above. The combination of these two recursive splitting ideas (splitting qubits according to the grid structure, and splitting the layers in half) gives a simulation strategy with the specified runtime.

A.4 Slicing

Assume we are given a quantum circuit $G = (V, E, \lambda)$ and a set of nodes $C \subseteq V$ with m interior hyperedges and n hyperedges that contain at least one node in C and one node outside C . Choose $s < n$ hyperedges that leave C , and assume that we want to perform a contraction of C with some other set of tensors C' . Trivially, we can contract C with computational cost $O(2^{n+m})$ and total memory cost

$O(2^n + m)$, create a rank n tensor, and then perform the contraction with C' .

An alternative way to perform computation that takes advantage of parallel computing capabilities is usually referred to as *slicing*. The idea is as follows: for all the 2^s possible values of the chosen s hyperedges, contract C with the value for these hyperedges fixed, creating 2^s “sliced” tensors. Calculating each of the sliced tensors has computational cost $O(2^{n+m-s})$ and memory (primary storage) cost $O(2^{n-s} + m)$. We can then contract each of the sliced tensors with C' . We remark that there are 2^s sliced tensors, and if we multiply the costs to compute the sliced tensors by 2^s we obtain essentially the initial cost for the contraction of C . However, there are two potential advantages to be gained through slicing: the more obvious one is that the 2^s computations can be performed in parallel; the less obvious, but equally important, is that we may be able to reorder the tensor computation in such a way that no more than a few slices of size $O(2^{n-s} + m)$ each have to be in primary storage at the same time — the smaller the slices, the higher in the memory stack they can be fit. Our simulation scheme makes this explicit by periodically storing or reading slices to/from (primary or secondary) storage. An appropriate slicing strategy can lead to significant memory savings by essentially splitting large tensors into smaller parts that can be processed separately.

A.5 Our simulation strategy

Given the framework defined above, the simulation strategy that we propose consists of partitioning the tensor network associated with the circuit into a small number of tensors with manageable rank and few hyperedges between tensors. Within each of these tensors, corresponding to subcircuits, we perform contraction in layers in a manner similar to that of the Schrödinger strategy. We provide below a more formal description. We assume here for simplicity that all output wires of the tensor network are open, i.e., connected to “O”, to output the full quantum state; if this is not the case, the upper bounds on memory costs given in this section can potentially be tightened depending on the structure of the quantum circuit. In terms of notation, given $W \subseteq V$, we define

$$\mathcal{C}[W] := \{e \in E : \exists u, v \in e \text{ such that } u \in W, v \notin W\},$$

i.e., the set of hyperedges crossing the boundary of W . With a slight abuse of notation, given $F \subseteq E$ and $W \subseteq V$, we denote by $W \setminus F := W \setminus \bigcup_{e \in F} e$; in other words, subtracting a set of edges F from a set of nodes W implies deleting from W the nodes appearing in F .

Partition the vertex set V of G into V_1, \dots, V_k , which we call “subcircuits”. For $i = 1, \dots, k$, let $E_i := \mathcal{C}[V_i]$ be the set of hyperedges that contain at least one node in V_i but are not fully contained in V_i . The computation is divided into $t \geq 1$ steps, with input/output operations from/to secondary storage between consecutive steps (although as we will discuss later, these operations may be skipped if all the intermediate tensors fit in primary storage). The sequence $\sigma_1, \dots, \sigma_k$ is a *computation order with t steps* if it is nondecreasing, $\bigcup_{i=1, \dots, k} \sigma_i = \{1, \dots, t\}$, and for every hyperedge e , denoting by $\{V_j\}_{j \in \Sigma_e}$ the ordered sequence of sets V_1, \dots, V_k with nonempty intersection with e , then the sequence $\{\sigma_j\}_{j \in \Sigma_e}$ is also nondecreasing. The numbers $\sigma_1, \dots, \sigma_k$ are called the *computation steps* of sets V_1, \dots, V_k . Since V_1, \dots, V_k is a partition, we can unambiguously assign to each node in V the computation step from the subcircuit it belongs to. This simplifies our exposition. According to this definition, every hyperedge is directed from lower-index computation steps to higher-index computation steps. Clearly there exists a computation order for any partition V_1, \dots, V_k , because $t = 1, \sigma_1 = \dots = \sigma_k = 1$ is valid. The special node “O” is assigned the final computation step index $t + 1$. For every $i = 1, \dots, k, v \in V_i$, we define $V(v) := V_i$ and $\sigma(v) = \sigma_i$.

The computation proceeds following the computation order $\sigma_1, \dots, \sigma_k$. Subcircuits contracted at a given computation step can be used to initialize tensors in subsequent computation steps if they meet certain requirements. Formally, we assume that a set $P \subset \{(i, j) : \sigma_j = \sigma_i + 1, i, j = 1, \dots, k\}$ of

precedence relations is given:

$$V_i \prec V_j \quad \forall (i, j) \in P.$$

The relation $V_i \prec V_j$ implies that subcircuit V_i can be used to initialize subcircuit V_j , therefore when V_j is processed the only open ranks in V_i must be those of the hyperedges that connect it to V_j . Let

$$\Delta := \{e \in E : \exists u, v \in e \text{ such that } \sigma(v) > \sigma(u) \text{ and } V(u) \not\prec V(v)\}.$$

In other words, Δ is the set of hyperedges linking subcircuits in different computation steps that do not follow the \prec relation. We give below in Algorithm 1 a pseudocode description of our simulation strategy. In the description, we call S the set of hyperedges sliced up until that point. All edges in Δ are sliced in the course of the algorithm.

Algorithm 1 Outline of the simulation strategy.

```

1:  $S \leftarrow \Delta \cap E_1$ .
2: for  $i = 1, \dots, k$  do
3:   for all combinations of values for the hyperedges in  $S$  do
4:     contract  $V_i$ , loading the initial state vector from secondary storage and following Schrödinger's
       method
5:     if  $\sigma_{i+1} > \sigma_i$  then
6:       contract all tensors in  $\{V_j : \sigma_j = \sigma_i\}$  and store the resulting tensor to secondary storage
7:     end if
8:   end for
9:    $S \leftarrow S \cup (\Delta \cap E_{i+1})$ 
10: end for

```

We now analyze the computational and storage requirements of the crucial steps of the algorithm.

Proposition. At step 4 of Algorithm 1, let

$$m_i := \left| \mathcal{C}[V_i \setminus \Delta] \setminus \bigcup_{j: \sigma_j < \sigma_i} E_j \right|,$$

and ℓ_i be the number of layers within V_i in the topological ordering of the circuit G . Then step 4 can be executed in $O(\ell_i 2^{m_i})$ time requiring $O(2^{m_i})$ primary storage.

Proof. Consider the first layer of V_i in the topological ordering of the graph. By definition, there are at most $|\mathcal{C}[V_i]|$ hyperedges crossing the boundary of such layer. Since edges in Δ are sliced (i.e., their value is fixed in every iteration of the for loop at line 3), the tensors appearing in Δ are one-dimensional and can be contracted in linear time without adding open ranks. We are left with the tensors in $V_i \setminus \Delta$, which can be contracted to a tensor of rank $\mathcal{C}[V_i \setminus \Delta]$. However, by construction all edges in $\bigcup_{j: \sigma_j < \sigma_i} E_j$ (i.e., edges coming from earlier layers of the circuit – notice that sliced edges are removed only once) connect V_i to a tensor that has already been fully contracted, and can be considered as the “initial state” of the first layer of V_i . Thus, the first layer of V_i is a tensor of rank at most m_i , which takes at most $O(2^{m_i})$ primary storage and $O(2^{m_i})$ time to construct. We can then proceed following the topological ordering, contracting each layer with the subsequent layer. Each such step requires $O(2^{m_i})$ time, and yields a tensor of size $O(2^{m_i})$. Overall, this implies that V_i can be contracted in time $O(\ell_i 2^{m_i})$ requiring $O(2^{m_i})$ primary storage, as indicated. ■

Proposition. At step 6 of Algorithm 1, let $C_i := \{V_j : \sigma_j = \sigma_i\}$ be the set of tensors to be contracted, $\Gamma_i := \{e \in E : \exists u, v \in e \text{ such that } u \in V_j, v \in V_h, j \neq h, V_j, V_h \in C_i\} \setminus \Delta$ the set of hyperedges to be contracted, and let $N_i := \{e \in E : \exists u, v \in e \text{ such that } \sigma(u) = \sigma_i \text{ and } \sigma(v) = \sigma_i + 1\} \setminus \Delta$ be the

Gate	Multiplications	Additions	Memory [bytes]
X	2^{n+1}	2^n	2^{n+4}
Y	2^{n+1}	2^n	2^{n+4}
Z	2^n	0	2^{n+4}
H	2^{n+1}	2^n	2^{n+4}
CX	2^{n+2}	$3 \cdot 2^n$	2^{n+4}
CZ	2^n	0	2^{n+4}

Table 2: Memory requirements and number of floating point of operations for some quantum gates, when applied to a n -qubit quantum state (2^n -dimensional double precision complex vector).

hyperedges acting as input to the next computation step that are not sliced. Then step 6 can be executed in $O(2^{|N_i|} + |\Gamma_i|)$ time requiring $O(\sum_{j \in C_i} 2^{m_j})$ primary storage and $O(2^{|N_i|})$ secondary storage.

Proof. Consider the hyperedges leaving C_i . Those hyperedges that do not intersect with subcircuits with computation step $\sigma_i + 1$ must be in Δ , hence their value is fixed by the for loop. Thus, at every iteration of the for loop, we must compute a tensor of rank $|N_i|$. To perform the contraction of the tensors corresponding to the subcircuits in $|C_i|$ we typically store the input tensors in primary storage, requiring $O(\sum_{j \in C_i} 2^{m_j})$ space, and perform $O(2^{|\Gamma_i|})$ operations per element of the output tensor. The output can be stored to secondary storage. This yields the memory and computation costs indicated in the statement of the proposition. ■

The two propositions above specify the memory and computational cost of the two main resource-intensive steps of Alg. 1. In principle, it might be possible to perform the computation in different ways that may be more efficient, hence our analysis only states upper bounds. We remark that the stated upper bounds hold for each iteration of the for loop for sliced hyperedges, hence to obtain the total computational and secondary storage cost one should multiply by $2^{|S|}$; however, primary storage requirements do not scale exponentially with $|S|$, because at every iteration of the for loop we can keep in memory only the tensors corresponding to the current values for sliced edges. Furthermore, the for loop can be parallelized very efficiently, as long as we ensure that all the tensor slices involved in a computation are available on a given compute node.

Based on the preceding analysis, our goal is to look for a decomposition of G into subcircuits so that the computational and memory requirements are as small as possible. The search for such a decomposition can be carried out in a heuristic manner, as described in the main text of the paper, or with exact algorithms, e.g., integer programming and branch-and-bound. Typically, the bottleneck for the simulation is given by primary storage requirements. Indeed, since each subcircuit is simulated essentially using Schrödinger's method (with some additional bookkeeping for ranks corresponding to hyperedges that connect to subcircuits with the same computation step), primary memory is the scarcest resource for our simulation strategy. Finally, from a practical point of view one should consider deviations from the proposed strategy that better fit the available hardware. For example, for the simulation of the 7×7 , depth-27 and 8×7 , depth-23 circuits discussed in the main text we do not need secondary storage at all: the tensors to be stored to disk all fit in primary storage (one slice at a time), therefore we speed up the computation by skipping the disk read/write cycle.

A.6 An example of possible computation schemes

We now provide a small example in order to illustrate the ideas discussed above. The memory and floating point requirements for the operations that will be used in this example are given in Table 2. Notice that these requirements assume that we want to compute the full state vector and each complex number requires 16 bytes of memory (two double-precision floating point numbers).

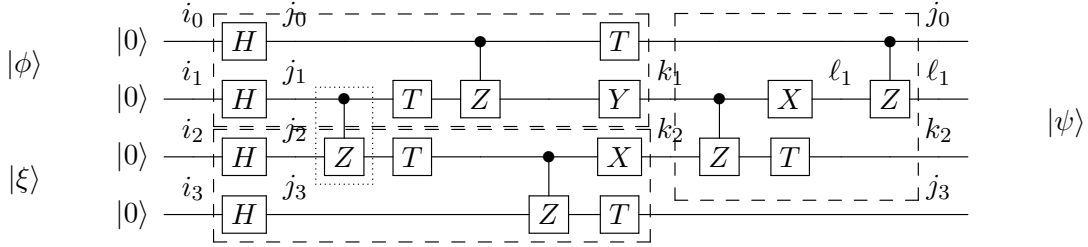


Figure 6: Example of a random 4×1 -qubit, depth 15 circuit generated according to [5]. The circuit can be contracted to 9 layers. The partitioning scheme is indicated in the figure. The tensor corresponding to the entangling gate in the second layer is assigned to the bottom subcircuit.

We consider a universal random circuit for a 4×1 grid of qubits with depth 15. It turns out that the generating rules produce many empty layers for this example and the circuit can be represented using 9 layers. Such a circuit is depicted in Fig. 6, together with a possible partitioning scheme. Using the notation described in the previous section, we have three subcircuits V_1, V_2, V_3 labeled $|\phi\rangle, |\xi\rangle, |\psi\rangle$ in Fig. 6. The computation order is $\sigma_1 = 1, \sigma_2 = 1, \sigma_3 = 2$; the precedence relations are $V_1 \prec V_3, V_2 \prec V_3$. The tensor for the first CZ gate in the circuit is assigned to V_2 , and there are three sliced hyperedges (indices j_0, k_2, j_3). To give a clearer description of how the proposed algorithm works, we give the full equations governing the state using the labeling indicated in the diagram (for simplicity, we use gate names to indicate the corresponding matrices):

$$\begin{aligned} \phi_{j_0 k_1 j_1} &= T_{j_0, j_0} Y_{k_1, j_1} CZ_{j_0 j_1, j_0 j_1} T_{j_1, j_1} \sum_{i_0 \in \{0,1\}} H_{j_0, i_0} \delta_{i_0} \sum_{i_1 \in \{0,1\}} H_{j_1, i_1} \delta_{i_1} \\ \xi_{j_1 k_2 j_3} &= T_{j_3, j_3} \sum_{j_2 \in \{0,1\}} X_{k_2, j_2} CZ_{j_2 j_3, j_2 j_3} T_{j_2, j_2} CZ_{j_1 j_2, j_1 j_2} \sum_{i_2 \in \{0,1\}} H_{j_2, i_2} \delta_{i_2} \sum_{i_3 \in \{0,1\}} H_{j_3, i_3} \delta_{i_3} \\ \psi_{j_0 \ell_1 k_2 j_3} &= CZ_{j_0 \ell_1, j_0 \ell_1} T_{k_2, k_2} \sum_{k_1 \in \{0,1\}} X_{\ell_1, k_1} CZ_{k_1 k_2, k_1 k_2} \sum_{j_1 \in \{0,1\}} \phi_{j_0 k_1 j_1} \xi_{j_1 k_2 j_3}. \end{aligned}$$

Note that, although the first CZ gate in the circuit is assigned to the bottom $|\xi\rangle$ subcircuit, we have to keep track of the extra j_1 index associated with that CZ gate in the top $|\phi\rangle$ subcircuit once the Y gate is introduced. In other words, j_1 becomes an entanglement index that cannot be contracted away until the tensors corresponding to the top $|\phi\rangle$ and bottom $|\xi\rangle$ subcircuits are combined: the precedence relations $V_1 \prec V_3, V_2 \prec V_3$ ensure that this is carried out before V_3 is computed. Because the hyperedges corresponding to indices j_0, k_2, j_3 are sliced, we never have to explicitly materialize the full state $|\psi\rangle$ in memory, and can work on slices. In this example, the final state can be computed in $2^3 = 8$ slices using a state vector of size 2^1 for the computation of a slice, never allocating memory to hold a full 2^4 -dimensional state vector. Furthermore, we can decide to keep each slice in primary storage skipping all the secondary storage input/output operations indicated in Alg. 1, as the size of an individual slice does not exceed the available primary storage space.

The partitioning scheme for the 7×7 , depth-27 and 8×7 , depth-23 circuits is akin to the above example. With a similar graphic scheme (some details are omitted due to the circuit size), we depict in Fig. 7 the partitioning scheme used for the depth-27 and depth-23 simulations discussed in the main text of the paper.

A.7 Computation of single amplitudes

The discussion so far has focused on the computation of the entire state vector, which is a natural outcome considering that our methodology is based on applying the Schrödinger approach to subcircuits. Computing a single amplitude $\langle x | Q | y \rangle$ for given basis states x, y is, in general, a simpler task. We can exploit the machinery described above to compute single amplitudes for circuits that are otherwise intractable with existing methodologies. In broad terms, we borrow inspiration from the recursive circuit

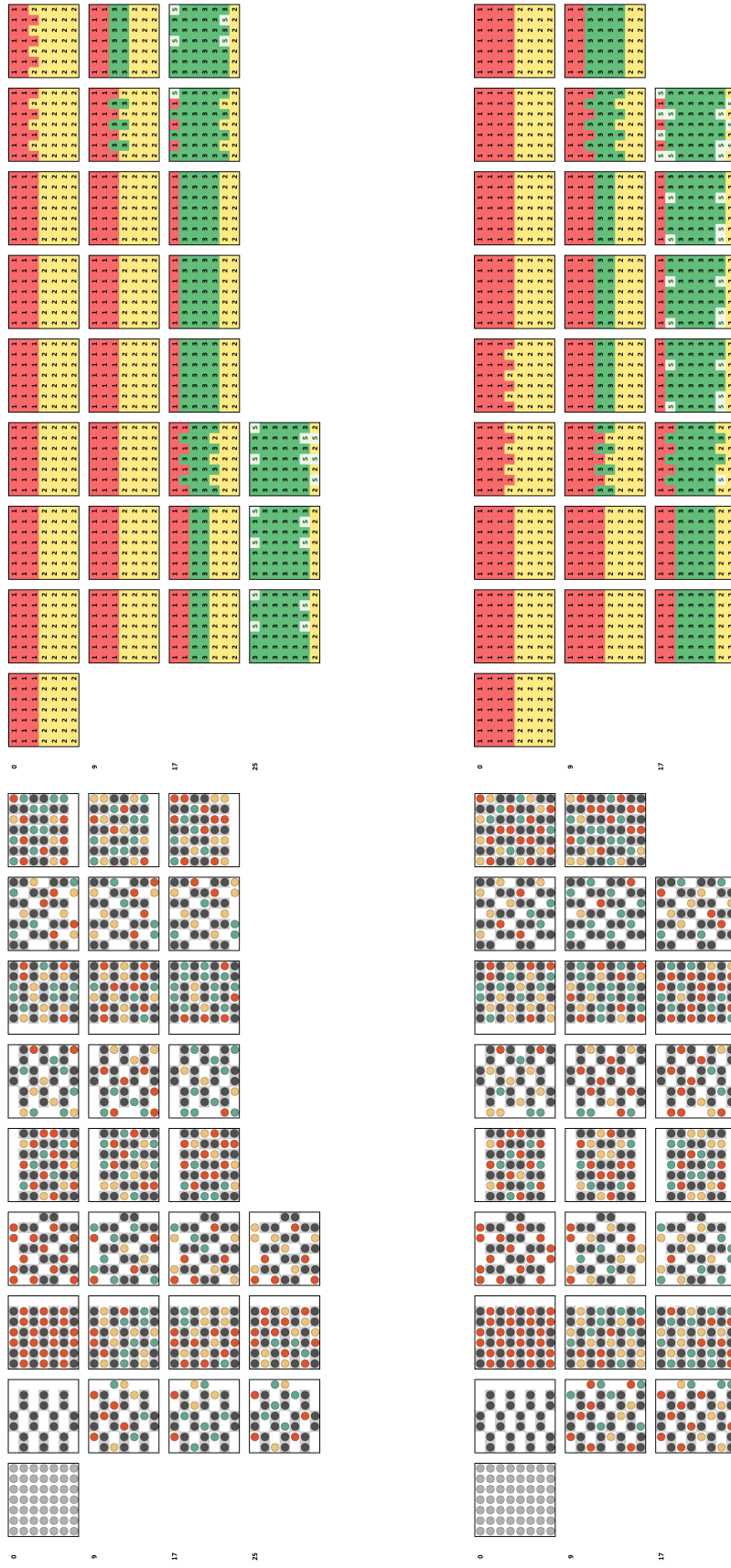


Figure 7: The 49-qubit, depth 27 circuit and the 56-qubit, depth 23 circuit are represented on the left. The figure on the right contains the respective partitioning. Qubits marked with an “S” can be sliced, as can the qubits in subcircuits 1 and 2 that are not involved in subcircuit 3 (i.e., those for which subcircuit 3 does not contain any gates applied to them).

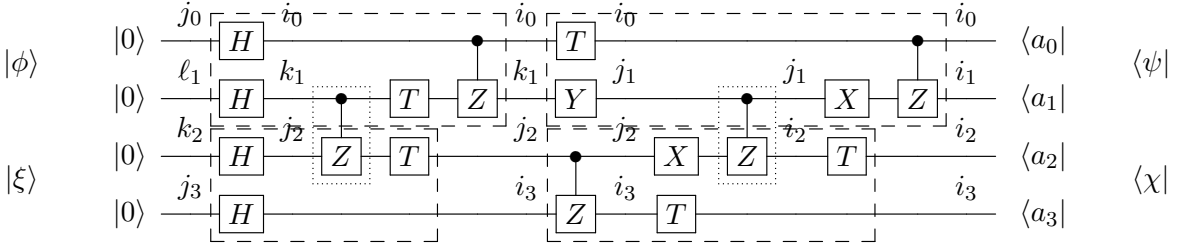


Figure 8: Example of a partitioning scheme to compute single amplitudes for the circuit in Fig. 6, simulating the circuit in input-to-output and output-to-input order. The tensors corresponding to the two dotted entangling gates are assigned to the top subcircuits.

partitioning schemes proposed in [1], but we depart from a purely recursive approach by constructing tensors for the resulting subcircuits using the computation scheme previously discussed.

Following [1], we first partition circuits depth-wise. Suppose we are given a quantum circuit of depth d implementing a unitary matrix Q . Calling L the unitary representing the first $\approx d/2$ layers of the circuit, and R the unitary representing the remaining layers, we have $Q = RL$. Our goal is to compute $\langle x | Q | y \rangle = \langle x | RL | y \rangle$. This can be accomplished by computing $L | y \rangle$ and $R^\dagger | x \rangle$ separately, then combining $(R^\dagger | x \rangle)^\dagger L | y \rangle$ to obtain $\langle x | RL | y \rangle$. Intuitively, this corresponds to simulating the circuit in input-to-output order for approximately half the total depth, and in output-to-input order for the remaining layers. The resulting tensors can then be contracted to obtain the desired amplitude. This idea was also developed, independently, in [23], but we contract the resulting tensors with a more efficient order than in [23].

We are interested in working with circuits whose state vectors cannot be fully stored in primary memory, so, in general, tensors corresponding to $L | y \rangle$ and $R^\dagger | x \rangle$ cannot be constructed directly. Instead, we apply the second partitioning scheme proposed in [1], which is to split the circuit row-wise. Assuming an $r \times c$ grid of qubits, the subcircuits corresponding to L and R would each be further partitioned into the top $\approx r/2$ rows of gates and the bottom remaining rows of gates. Following the approach described earlier, entanglement gates that bridge these top and bottom partitions would be assigned to one partition or the other, with entanglement indices introduced as appropriate. This assignment affects the memory requirements, therefore it is preferable to assign bridging gates to partitions so as to minimize the resulting memory occupation.

If ϕ and ξ are the top and bottom tensors constructed for the subcircuit corresponding to L , and if ψ and χ are the corresponding tensors for R , then contracting ϕ and ξ yields $L | y \rangle$ and contracting ψ and χ yields $R^\dagger | x \rangle$. Contracting all four tensors thus yields the desired amplitude $\langle x | RL | y \rangle$. Because we have complete freedom to choose the order of contraction, we can also consider contracting ϕ and ψ separately from ξ and χ , and then contracting the resulting tensors. This last order of contraction has desirable properties in terms of both memory requirements and floating-point operations.

Fig. 8 illustrates these ideas on the same circuit used for one of our previous examples. We give below the equations describing each of the subcircuits involved in the figure. In these equations, indices j_2 and i_2 correspond to the hyperedges of the CZ gates connecting the two wires in the middle that remain “open” in the corresponding tensor (i.e., not contracted within the tensor).

$$\begin{aligned}
\phi_{i_0 k_1 j_2} &= CZ_{i_0 k_1, i_0 k_1} T_{k_1, k_1} CZ_{k_1 j_2, k_1 j_2} \sum_{j_0 \in \{0,1\}} H_{i_0, j_0} \delta_{j_0} \sum_{\ell_1 \in \{0,1\}} H_{k_1, \ell_1} \delta_{\ell_1} \\
\xi_{j_2 i_3} &= T_{j_2, j_2} \sum_{k_2 \in \{0,1\}} H_{j_2, k_2} \delta_{k_2} \sum_{j_3 \in \{0,1\}} H_{i_3, j_3} \delta_{j_3} \\
\psi_{i_0 k_1 i_2} &= \left(\sum_{j_1 \in \{0,1\}} X_{i_1, j_1} CZ_{j_1 i_2, j_1 i_2} Y_{j_1, k_1} \right) T_{i_0, i_0} CZ_{i_0 i_1, i_0 i_1} \delta_{i_0 - a_0} \delta_{i_1 - a_1} \\
\chi_{j_2 i_3 i_2} &= CZ_{j_2 i_3, j_2 i_3} X_{i_2, j_2} T_{i_3, i_3} T_{i_2, i_2} \delta_{i_2 - a_2} \delta_{i_3 - a_3}
\end{aligned}$$

Given these four subcircuits, there are two natural ways to combine them to obtain the desired amplitude

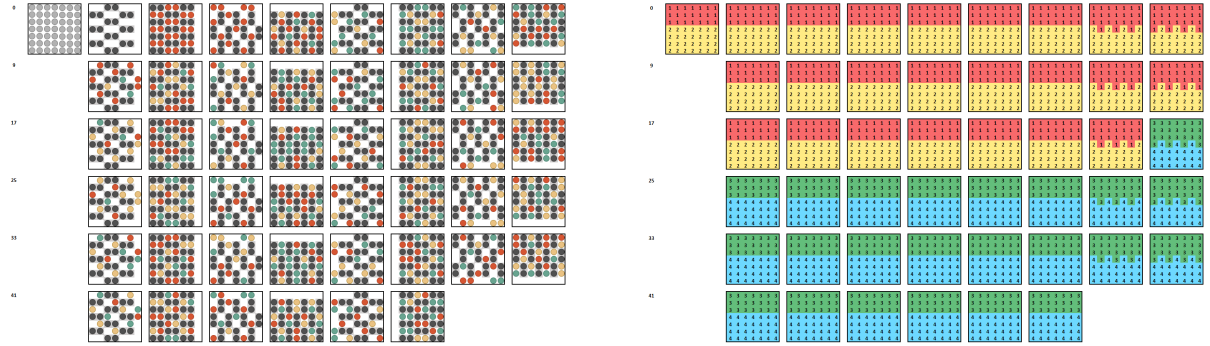


Figure 9: A 49-qubit, depth 46 circuit (left) and its partitioning (right).

α : we can combine the tensors “vertically” first ($|\phi\rangle$ with $|\xi\rangle$, and $\langle\psi|$ with $\langle\chi|$) to obtain

$$\begin{aligned}\lambda_{i_0 k_1 j_2 i_3} &= \sum_{j_2 \in \{0,1\}} \phi_{i_0 k_1 j_2} \xi_{j_2 i_3} \\ \rho_{i_0 k_1 j_2 i_3} &= \sum_{i_2 \in \{0,1\}} \psi_{i_0 k_1 i_2} \chi_{j_2 i_3 i_2} \\ \alpha &= \sum_{i_0, k_1, j_2, i_3 \in \{0,1\}} \lambda_{i_0 k_1 j_2 i_3} \rho_{i_0 k_1 j_2 i_3},\end{aligned}$$

or “horizontally” first ($|\phi\rangle$ with $\langle\psi|$, and $|\xi\rangle$ with $\langle\chi|$) to obtain

$$\begin{aligned}\sigma_{i_2 j_2} &= \sum_{i_0, k_1 \in \{0,1\}} \phi_{i_0 k_1 j_2} \psi_{i_0 k_1 i_2} \\ \omega_{i_2 j_2} &= \sum_{j_2, i_3 \in \{0,1\}} \xi_{j_2 i_3} \chi_{j_2 i_3 i_2} \\ \alpha &= \sum_{i_2, j_2 \in \{0,1\}} \sigma_{i_2 j_2} \omega_{i_2 j_2}.\end{aligned}$$

It is easy to verify that the second approach is more efficient, creating intermediate tensors with smaller memory footprints and requiring fewer floating point operations.

We now describe a way to compute single amplitudes of universal random circuits with ~ 50 qubits and depth > 40 , which until very recently was thought to be out of reach for current technology. We discuss here the calculation of single amplitudes for a 7×7 -qubit, depth 46 universal random circuit. As discussed in the example above, we partition the circuit into four subcircuits: two depth-23 subcircuits simulated in an input-to-output fashion, which correspond to the first 23 layers and layer 0, and two depth-23 subcircuits simulated output-to-input, which correspond to the remaining 23 layers. Both pairs of subcircuits are partitioned at the boundary between the third and fourth rows of qubits, with the CZ gates that bridge this boundary assigned to the top subcircuit in each pair. This partitioning is illustrated in Fig. 9.

The four tensors constructed for these four subcircuits will incorporate various subsets of indices. One of these subsets of indices represents the quantum state of the qubits after applying the gates in layers 0 through 23. Let q_1, \dots, q_{49} be these indices with qubits numbered in left-to-right, top-to-bottom order. Fourteen additional entanglement indices also need to be introduced in the tensors representing layers 0 through 23 to account for the deferred contraction of the CZ gates that bridge the third and fourth rows in layers 7, 8, 15, and 16. Let e_1, \dots, e_{14} be these indices. Similarly, 14 additional entanglement indices need to be introduced in the tensors representing the remaining 23 layers to account for the deferred contraction of the CZ gates that bridge the third and fourth rows in layers 31, 32, 39, and 40. Let e_{15}, \dots, e_{28} be these indices. Because CZ gates are diagonal, additional entanglement indices are not needed for the bridging CZ gates at depths 23 and 24. Instead, q_{22}, \dots, q_{28} serve as these entanglement indices.

Following the nomenclature used in the above example, the four tensors calculated from the four subcircuits are then:

1. $\phi_{q_1 \dots q_{21} e_1 \dots e_{14} q_{23} q_{25} q_{27}}$ corresponding to the “top-left” subcircuit, requiring 4 TB of storage in double precision;
2. $\xi_{q_{22} \dots q_{49} e_1 \dots e_{14}}$ corresponding to the “bottom-left” subcircuit, requiring 64 TB of storage in double precision;
3. $\psi_{q_1 \dots q_{21} e_{15} \dots e_{28} q_{22} q_{24} q_{26} q_{28}}$ corresponding to the “top-right” subcircuit, requiring 8 TB of storage in double precision;
4. $\chi_{q_{22} \dots q_{49} e_{15} \dots e_{28}}$ corresponding to the “bottom-right” subcircuit, requiring 64 TB of storage in double precision;

Note that the total memory requirement of 140 TB for these four tensors lies well within the limits of existing supercomputers. The horizontal-first contraction of the two top tensors and the two bottom tensors yields two intermediate tensors of 0.5 TB each, and the final amplitude calculation amounts to a complex-valued dot product:

$$\begin{aligned}\sigma_{q_{22} \dots q_{28} e_1 \dots e_{28}} &= \sum_{q_1, \dots, q_{21} \in \{0,1\}} \phi_{q_1 \dots q_{21} e_1 \dots e_{14} q_{23} q_{25} q_{27}} \psi_{q_1 \dots q_{21} e_{15} \dots e_{28} q_{22} q_{24} q_{26} q_{28}} \\ \omega_{q_{22} \dots q_{28} e_1 \dots e_{28}} &= \sum_{q_{29}, \dots, q_{49} \in \{0,1\}} \xi_{q_{22} \dots q_{49} e_1 \dots e_{14}} \chi_{q_{22} \dots q_{49} e_{15} \dots e_{28}} \\ \alpha &= \sum_{q_{22}, \dots, q_{28}, e_1, \dots, e_{28} \in \{0,1\}} \sigma_{q_{22} \dots q_{28} e_1 \dots e_{28}} \omega_{q_{22} \dots q_{28} e_1 \dots e_{28}}.\end{aligned}$$

Although we have not carried out the above simulations, expected execution times can nevertheless be estimated in a safe way (i.e., overestimated) by first developing parallelization schemes for the computations, then generating and testing benchmark codes that provide upper bounds on the computational loads per processing node for each subtask, and finally combining these execution times with estimated communication times based on the communication patterns and data transfer volumes dictated by the parallelization schemes. The estimated run times based on this methodology are 17.93 hours on the Vulcan supercomputer described earlier, and 4.76 hours on Sequoia, an IBM Blue Gene/Q supercomputer also located at Lawrence Livermore National Laboratory that is $4 \times$ the size of Vulcan. To obtain safe upper bounds on the expected runtime, the benchmark codes responsible for 98.7% of the estimated times did not employ high-performance computing techniques such as cache blocking and loop unrolling. Faster run times should be achievable in actual, well-engineered implementations.

The recent paper [23] describes the computation of a single amplitude for a 7×7 , depth 55 circuit, using the idea of simulating the circuit in input-to-output order for approximately half the total depth, and in output-to-input order for the remaining layers. Once the two halves $L|y\rangle$ and $R^\dagger|x\rangle$ of the circuit are simulated, [23] computes the dot product $(R^\dagger|x\rangle)^\dagger L|y\rangle$ in slices in the most direct way, without changing the order of the tensor computation as discussed in this paper to reduce resource consumption. Such reordering does not appear to be necessary in the case of [23], likely because it uses a supercomputer (Sunway TaihuLight, ranked 1st in the TOP500 list of supercomputers as of November 2017) with significantly more memory than Vulcan or Sequoia.

A.8 Leveraging secondary storage

The paper [19] suggests that solid-state disk, or more generally secondary storage, could be used to supplement main memory in order to simulate circuits whose quantum states are too large to store in main memory alone. We combine the methods presented here with those in [19] to describe a viable computation scheme that exploits secondary storage to simulate deeper circuits than was thought possible.

The two methodologies are related by the fact that both involve circuit partitioning and both employ tensor slicing. In the case of [19], “global” qubits used to index across processing nodes correspond to tensor indices that are being sliced, and “local” qubits correspond to tensor indices that are being used to

index into tensor slices stored on each processing node. In [19], circuits are partitioned so that all gates within a subcircuit can be applied to update quantum state tensors on a per-slice basis without communicating quantum state information between processing nodes. Zero-communication updates are possible when all non-diagonal gates in a subcircuit are being applied to “local” qubits only. Such updates are also possible for a handful of additional circumstances described in [19]. In effect, circuits are partitioned by selecting different subsets of “local” qubits and analyzing which gates can be applied to yield corresponding subcircuits. During simulation, communication between processing nodes occurs only when the simulation switches from one subcircuit to another. During these communication phases, the memory layouts of quantum state tensors are reorganized so that new subsets of indices are being used to “globally” index across processing nodes versus “locally” index within the memories of individual nodes, according to the needs of the next subcircuit to be simulated.

In the methods presented earlier, we considered circuit partitionings in which the resulting tensors either fit in available aggregate primary memory in their entirety, or slices of the resulting tensors could be computed using available primary memory based on other tensors already computed and stored in primary memory. The resulting tensors and/or their slices will generally be larger than the primary memories of individual processing nodes, which represents a difference in the way tensor slicing is being viewed in this paper as compared to [19]. The techniques presented in [19] can be combined with those presented here to employ secondary storage when quantum states are too large to fit in aggregate primary memory. Because secondary storage is typically orders of magnitude slower than main memory, the viability of using it depends on the extent to which the number of read/write cycles can be minimized or overlapped with computation. To achieve such minimization, we first employ our decomposition ideas to partition the initial portions of a circuit so as to maximize the number of gates that can be simulated using available aggregate memory, with the resulting quantum state then calculated in slices and written to secondary storage. The partitioning methods discussed in [19] can then be applied to the remaining gates in the circuit with the number of “local” qubits set higher, according to the size of aggregate memory instead of the memory size available on individual processing nodes. The resulting tensor slices will then be much larger, allowing many more gates to be simulated before additional secondary-storage read/write cycles are needed. The resulting subcircuits can then be further partitioned into sub-subcircuits to minimize internode communication in the overall calculations.

We now provide a specific implementation of the above idea and estimate its computational cost. Simulating universal random circuits of ~ 50 qubits with arbitrary depth using secondary storage results in higher execution times due to the relatively high cost of disk read/write operations. However, we find both that the slowdown is considerably less than twofold for the instances under study, and that recent system advancements, such as NVRAM-based burst buffers, can have a highly beneficial effect on these run times. The larger memory pool available via secondary storage allows us to push the boundary of quantum circuit simulations even further. In order to do so, we observe that, by construction, universal random circuits have groups of qubits on the boundary of the grid that periodically do not interact with other qubits for several layers of gates. In particular, for circuits on a 7×7 grid, a group of 7 qubits at the boundary has two layers of two-qubit interactions with other rows or columns, followed by six layers without further interactions (only single-qubit gates or two-qubit gates within the group). For this reason, slicing these qubits is very effective: we can choose one of the boundary rows or columns, slice the corresponding qubits for six layers, and simulate the circuit applied to the remaining qubits independently. Recently [19] used a similar observation to decide how to distribute computation across processors.

Our strategy consists in the following. We slice qubits at the boundary of the grid (e.g., the bottom row of the grid), simulating the remaining part of the circuit using Schrödinger’s method with a tensor as large as our memory allows. The simulation is carried out for as many layers of gates as possible without introducing additional entanglement indices. Remarkably, for qubits on the opposite row/column (e.g.,



Figure 10: Partitioning of a 49-qubit, depth 83 circuit.

the top row of the grid) this allows us to apply over 30 layers of gates, whereas for qubits closer to the sliced qubits we can only progress for a handful of layers before we are forced to stop or increase memory occupancy. This produces several slices of the same size, which are stored to disk. To apply further gates we start a new subcircuit, slicing qubits in the row/column opposite to those sliced in the previous subcircuit (e.g., the top row of the grid), and simulating the rest of the circuit with Schrödinger’s method. The initial state can be loaded from the slices stored on disk, and the process can be iterated. This yields a “wave” pattern in the subcircuits: each subcircuit starts from the top or bottom row of qubits, then extends to the rest of the circuit until it encompasses the row opposite to the starting set of qubits, at which point it shrinks back. We show the proposed circuit partitioning in Fig. 10. The specific example of Fig. 10 uses a circuit with depth 83, but the pattern used for subcircuits 4, 5 and 6 can be carried out indefinitely, adding further disk read/write operations. In the language of Alg. 1, there are 5 subcircuits: V_1, \dots, V_5 labeled 1, …, 5 in Fig. 10; we assign $\sigma_1 = \sigma_2 = 1, \sigma_3 = 2, \sigma_4 = 3, \sigma_5 = 4$, with precedence $V_1 \prec V_3, V_2 \prec V_3, V_3 \prec V_4, V_4 \prec V_5$. For every subcircuit $V_i, i \geq 3$, a row of qubits is sliced because the corresponding hyperedges connect V_{i-1} to V_{i+1} (if any non-diagonal single-qubit gates are applied on these qubits, instead of just one hyperedge per qubit we could have several shorter ones, which we would also slice).

For circuits of this size, it is important that the simulation algorithm is well-engineered in all of its aspects. Thus, we describe here the implementation choices that we used to estimate run times. We discuss a depth-83 circuit; the tables provide data for a depth-55 circuit as well.

Subcircuit	Num Gates	Compute Time (hours)	All-to-All Time (hours)	Total (hours)
1	215	0.00	0.00	0.00
2	336	0.00	0.01	0.01
Contract		0.39	0.00	0.39
3	621	0.94	3.05	3.98
4	346	0.52	2.03	2.55
Total	1518	1.85	5.08	6.93

Table 3: Estimated computation and communication times for a 7×7 -qubit, depth 55 random circuit simulated on the equivalent of 4096 nodes of a Cori-II-class supercomputer. Time estimates do not include secondary storage access.

Tensors for V_1 and V_2 in Fig. 10 are the first to be calculated, and the resulting pair of tensors is contracted one slice at a time. The slicing process proceeds by looping over the possible values for qubits 43–49 and slicing the tensor for V_2 on these values prior to performing the contraction with the tensor for V_1 . For each of the 128 resulting slices, the gates belonging to V_3 in Fig. 10 are applied to the contraction results and the resulting updated slices are transferred to secondary storage. This process of slicing, contracting, applying gates, and sending results to secondary storage is repeated 128 times, once for each of the 128 possible values of qubits 43–49. The gates belonging to V_4 in Fig. 10 are applied to the intermediate results that were transferred to secondary storage. These gate applications can also be performed in slices, this time slicing on qubits 1–7. To ensure the retrieval from secondary storage is performed efficiently, data can be organized in secondary storage as 2^{14} logical files indexed by the values of qubits 1–7 and 43–49, wherein each logical file contains 2^{35} complex amplitudes corresponding to qubits 8–42. Thus, in the phase discussed above of applying gates in V_3 , for each of the 128 values of qubits 43–49 that are being sliced, 128 logical files are written to secondary storage, corresponding to the 128 possible values of qubits 1–7. In the phase that applies the gates in V_4 , for each of the 128 values of qubits 1–7 that are being sliced, 128 logical files are read from secondary storage, corresponding to the 128 possible values of qubits 43–49. Once these 128 files of amplitudes are loaded into memory, the gates in V_4 can be applied and each updated slice can be written back to storage; alternatively, the final amplitudes can be processed in-memory on a per-slice basis.

For a depth-55 circuit, the simulation process ends with V_4 (in fact, we only need to apply the gates in V_4 at depth ≤ 55). To continue the simulation to depth 83, we repeat the process for V_5 , shown in Fig. 10, to simulate the remaining gates. We proceed in the same manner as for V_4 , except this time, for each of the 128 values of qubits 43–49 that are now being sliced, 128 logical files are loaded from secondary storage corresponding to the 128 possible values of qubits 1–7.

The timing results in [19] can be used to estimate computation and communication times for the above calculations, assuming that the parallelization methods discussed in [19] are being used and one is running on the equivalent of 4096 nodes of a Cori-II-class supercomputer. These times are reported in Tables 3 (for depth 55) and 4 (for depth 83).

The estimated compute times for V_1 and V_2 presented in Tables 3 and 4 are obtained by scaling the 6×5 -qubit simulation times reported in Table 1 in [19] according to the number of gates. The tensor values for V_1 and V_2 can be calculated in an embarrassingly parallel fashion without communication, where the local tensors in each node have rank 28. Thus, a single-node, 30-qubit simulation provides an upper bound to these compute times.

Estimated compute times for all other rows in Tables 3 and 4 are obtained by using the percent-communication column reported in Table 1 in [19] to first decompose the reported simulation time for a

Subcircuit	Num Gates	Compute Time (hours)	All-to-All Time (hours)	Total (hours)
1	215	0.00	0.00	0.00
2	336	0.00	0.01	0.01
Contract		0.39	0.00	0.39
3	618	0.93	3.05	3.98
4	756	1.14	3.05	4.19
5	348	0.53	2.03	2.56
Total	2273	2.99	8.13	11.12

Table 4: Estimated computation and communication times for a 7×7 -qubit, depth 83 random circuit simulated on the equivalent of 4096 nodes of a Cori-II-class supercomputer. Time estimates do not include secondary storage access.

Storage System	Size (PB)	Transfer Rate (TB/sec)	Single Precision (hours)	Double Precision (hours)
Summit Burst Buffer	7	10.00	0.23	
Summit File System	250	2.20	1.03	2.07
Sequoia File System	50	0.83	2.74	5.48
Vulcan File System	5	0.11	21.18	

Table 5: Secondary storage sizes available on certain IBM supercomputers, the corresponding transfer rates, and the times needed to write 2^{49} quantum amplitudes to secondary storage and then read them back assuming full sustained transfer rates. Summit is the IBM-Power9/NVIDIA-Volta supercomputer currently being installed at the Oak Ridge National Laboratory.

7×6 -qubit circuit into a per-gate compute time and a per-all-to-all communication and synchronization time. This per-gate compute time is scaled multiplying by the number of gates in each of the subcircuits under consideration, and then further multiplying by the number of slices (i.e., 128). The 7×6 timing results reported in [19] are used because subcircuits 3, 4, and 5 in Fig. 10 correspond to 7×6 -qubit subcircuits and the tensor slices involved in their simulation have rank 42. The sliced tensor contraction results for V_1 and V_2 also have rank 42. These tensor contractions require 128 complex multiplies and 127 complex additions per amplitude. An upper bound to the compute time is estimated by assuming an equivalent circuit-size of 256 gates to model the execution time.

All-to-all communication and synchronization times are estimated using the decomposed per-all-to-all time discussed above together with Figure 5 in [19] to determine the number of all-to-all communication cycles that are needed as a function of the depths of each subcircuit. Accordingly, for a depth 55 circuit, V_3 should require three all-to-alls per slice, while V_4 should require only two all-to-alls per slice. Similarly, for a depth 83 circuit, V_3 and V_4 should each require three all-to-alls per slice, while V_5 should require only two all-to-alls per slice. In addition, one all-to-all would be needed after computing the tensor for V_2 to redistribute it in preparation for the contraction of V_1 and V_2 . Each of these sources of all-to-all communication are reflected in Tables 3 and 4.

Tables 6-7 shows estimated overall run times, obtained by combining Tables 5, 3 and 4. We remark that these estimations assume the equivalent of 4096 of Cori II's 9304 compute nodes. Because Sequoia and Summit are both ranked faster than Cori II in terms of their High Performance Linpack benchmarks, these execution times should be achievable on both Sequoia and Summit, and they can likely be improved upon. Vulcan is four time smaller than Sequoia and so the computation and communication

Storage System	Compute (hours)	All-to-All (hours)	Single Precision Read/Write (hours)	Double Precision Read/Write (hours)	Single Precision Total (hours)	Double Precision Total (hours)
Summit Burst Buffer	1.85	5.08	0.23	–	7.16	–
Summit File System	1.85	5.08	1.03	2.07	7.97	9.00
Sequoia File System	1.85	5.08	2.74	5.48	9.68	12.42
Vulcan File System	7.40	20.33	21.18	–	48.92	–

Table 6: Estimates of total run times, including secondary storage read/write times, for the computation of the full state vector of a 7×7 , depth-55 circuit.

Storage System	Compute (hours)	All-to-All (hours)	Single Precision Read/Write (hours)	Double Precision Read/Write (hours)	Single Precision Total (hours)	Double Precision Total (hours)
Summit Burst Buffer	2.99	8.13	0.46	–	11.58	–
Summit File System	2.99	8.13	2.07	4.14	13.19	15.26
Sequoia File System	2.99	8.13	5.48	10.97	16.60	22.09
Vulcan File System	11.97	32.52	42.37	–	86.85	–

Table 7: Estimates of total run times, including secondary storage read/write times, for the computation of the full state vector of a 7×7 , depth-83 circuit.

times estimated for Sequoia were multiplied by four to produce entries for Vulcan. The above estimates are thus very safe. The secondary storage transfer time estimates are less safe, being solely based on published data transfer rates.

It should be noted that the overall run time estimates in Tables 6-7 are all dominated by the computation and communication times, and not the secondary storage transfer times. Because these secondary storage transfer times are not dominant, we can conclude that secondary storage provides a viable basis for simulating quantum circuits to arbitrary depth when quantum states are too large to fit in main memory alone. This concludes our analysis of computing times for deep circuits.

A.9 On the graph representation of two-qubit gates

The tensor network representation used in our paper differs from [25] because of the presence of hyperedges. As discussed in the main text, this leads to a more accurate computation of the size of the tensors for diagonal gates, and allows more efficient circuit graph decompositions. As it turns out, our representation is equivalent to that of [6]. This is now explained in more detail.

We consider a two-qubit diagonal gate, since this is the only case in which differences between our paper and [25] arise. This difference is also the reason we sometimes choose to transform CX gates into CZ gates and Hadamards, to take advantage of the more efficient treatment of the diagonal CZ gates. The complexity of the simulation algorithm described in [25] depends on the treewidth of the line graph of the circuit graph. Given a hypergraph $G = (V, E)$, its line graph $G^* = (V^*, E^*)$ is defined by the vertex set $V^* := \{e \in E\}$ and the edge set $E^* := \{(e^1, e^2) \in V^* \times V^* : e^1 \cap e^2 \neq \emptyset\}$. Notice that this definition matches the traditional definition of line graphs when applied to a regular graph G (as opposed to a hypergraph). We show the difference between the line graph of our representation of the graph circuit, and that of [25], using the circuit given in Fig. 11. The hypergraph of the circuit in Fig. 11

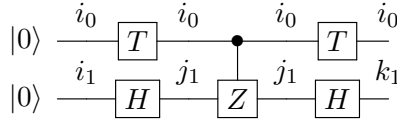


Figure 11: Example circuit for the line graph discussion.

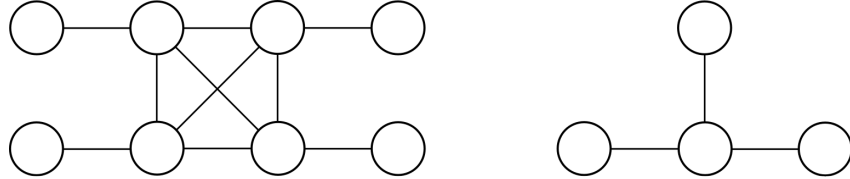


Figure 12: Line graph of the circuit in Fig. 11, using traditional tensor networks (left), and using the graphical model advocated in this paper (right).

has only four hyperedges because there are four different index labels in the circuit, while the traditional tensor network representation has eight — one for each wire segment. This leads to a 4-clique in the line graph of the traditional tensor network (Fig. 12, left), while the line graph of the hypergraph has only 2-cliques (Fig. 12, right). The reader can easily verify that the graphical model proposed in [6] in the context of a variable elimination algorithm yields exactly the same graph representation of the line graph of the hypergraph. This is due to the fact that both our hypergraph and the variable elimination model put more emphasis on the indices of the tensor network than in [25].

A.10 Derivation of the log-transformed outcome probabilities

In this section, we derive the expression for the distribution of $\log(Np)$ used in the main text. Let p be a random variable representing the probability of a randomly selected measurement outcome of a (pseudo) randomly generated universal quantum circuit of sufficient depth.

It is known [5] that as the depth increases, the distribution of p converges to a truncated exponential (a.k.a., Porter-Thomas [28]) distribution:

$$f_p(p) = \begin{cases} \frac{Ne^{-Np}}{1-e^{-N}} & \text{if } 0 \leq p \leq 1 \\ 0 & \text{otherwise} \end{cases}$$

Let the actual measurement probability with respect to the physical realization of the circuit, with circuit fidelity α be

$$q = \alpha p + \frac{1-\alpha}{N}.$$

The cumulative distribution of p is given by:

$$F_p(p) = \begin{cases} \frac{1-e^{-Np}}{1-e^{-N}} & \text{if } 0 \leq p \leq 1 \\ 0 & \text{if } p < 0 \\ 1 & \text{otherwise.} \end{cases}$$

The cumulative distribution of q is given by:

$$F_q(q) = F_p\left(\frac{1}{\alpha}\left(q - \frac{1-\alpha}{N}\right)\right) = \begin{cases} \frac{1-e^{-\frac{N}{\alpha}(q-\frac{1-\alpha}{N})}}{1-e^{-N}} & \text{if } \frac{1-\alpha}{N} \leq q \leq \alpha + \frac{1-\alpha}{N} \\ 0 & \text{if } q < \frac{1-\alpha}{N} \\ 1 & \text{otherwise.} \end{cases}$$

Hence, the probability density of q is:

$$f_q(q) = \frac{d}{dq} F_q(q) = \begin{cases} \frac{\frac{N}{\alpha} e^{-\frac{N}{\alpha}(q-\frac{1-\alpha}{N})}}{1-e^{-N}} & \text{if } \frac{1-\alpha}{N} \leq q \leq \alpha + \frac{1-\alpha}{N} \\ 0 & \text{otherwise} \end{cases}$$

In our own experiments working with 49-qubit and 56-qubit circuits, we found it convenient to plot the distribution of $\log(Nq)$ to better visualize the shape of this distribution over several orders of magnitude of variation in the value of Nq . We therefore first derive the distribution w.r.t. Nq , and then w.r.t. $\log Nq$. Let $x = Nq$. The cumulative distribution of x is:

$$F_x(x) = F_q\left(\frac{x}{N}\right) = \begin{cases} \frac{1-e^{-\frac{1}{\alpha}(x+\alpha-1)}}{1-e^{-N}} & \text{if } 1-\alpha \leq x \leq 1+(N-1)\alpha \\ 0 & \text{if } x < 1-\alpha \\ 1 & \text{otherwise.} \end{cases}$$

Thus, the probability density of x is:

$$f_x(x) = \frac{d}{dx} F_x(x) = \begin{cases} \frac{\frac{1}{\alpha} e^{-\frac{1}{\alpha}(x+\alpha-1)}}{1-e^{-N}} & \text{if } 1-\alpha \leq x \leq 1+(N-1)\alpha \\ 0 & \text{otherwise.} \end{cases}$$

Finally, let $z = \log(Nq) = \log(x)$. The cumulative distribution of z is:

$$F_z(z) = F_x(e^z) = \begin{cases} \frac{1-e^{-\frac{1}{\alpha}(e^z+\alpha-1)}}{1-e^{-N}} & \text{if } 1-\alpha \leq e^z \leq 1+(N-1)\alpha \\ 0 & \text{if } e^z < 1-\alpha \\ 1 & \text{otherwise.} \end{cases}$$

The probability density of z is therefore:

$$f_z(z) = \frac{d}{dz} F_z(z) = \begin{cases} \frac{\frac{1}{\alpha} e^{z-\frac{1}{\alpha}(e^z+\alpha-1)}}{1-e^{-N}} & 1-\alpha \leq e^z \leq 1+(N-1)\alpha \\ 0 & \text{otherwise} \end{cases} \quad (3)$$

With perfect circuit fidelity (i.e., $\alpha = 1$), Eq. 3 becomes a truncated Gumbel distribution that closely matches the empirical distributions obtained in our 49-qubit and 56-qubit simulations.

References

- [1] S. Aaronson and L. Chen. Complexity-theoretic foundations of quantum supremacy experiments. *arXiv preprint arXiv:1612.05903*, 2016.
- [2] R. J. Bartlett. Many-body perturbation theory and coupled cluster theory for electron correlation in molecules. *Annual Review of Physical Chemistry*, 32(1):359–401, 1981.
- [3] D. Bienstock and M. A. Langston. Algorithmic implications of the graph minor theorem. *Handbooks in Operations Research and Management Science*, 7:481–502, 1995.
- [4] L. S. Bishop, S. Bravyi, A. Cross, J. M. Gambetta, and J. Smolin. Quantum volume. Technical report, IBM T.J. Watson, 2017.
- [5] S. Boixo, S. V. Isakov, V. N. Smelyanskiy, R. Babbush, N. Ding, Z. Jiang, M. J. Bremnen, J. M. Martinis, and H. Neven. Characterizing quantum supremacy in near-term devices. *Nature Physics*, 2018.

- [6] S. Boixo, S. V. Isakov, V. N. Smelyanskiy, and H. Neven. Simulation of low-depth quantum circuits as complex undirected graphical models. *arXiv preprint arXiv:1712.05384*, 2017.
- [7] O. Buerschaper, M. Aguado, and G. Vidal. Explicit tensor network representation for the ground states of string-net models. *Physical Review B*, 79(8):085119, 2009.
- [8] D. Castelvecchi. Quantum cloud goes commercial. *Nature*, 543, 2017.
- [9] D. Castelvecchi. Quantum computers ready to leap out of the lab in 2017. *Nature*, 541:9–10, 2017.
- [10] J. Chen, F. Zhang, M. Chen, C. Huang, M. Newman, and Y. Shi. Classical simulation of intermediate-size quantum circuits. *arXiv preprint arXiv:1805.01450*, 2018.
- [11] Z. Chen, Q. Zhou, C. Xue, X. Yang, G. Guo, and G. Guo. 64-qubit quantum circuit simulation. *arXiv preprint arXiv:1802.06952*, 2018.
- [12] L. Dagum and R. Menon. OpenMP: an industry standard API for shared-memory programming. *IEEE computational science and engineering*, 5(1):46–55, 1998.
- [13] E. Farhi and A. W. Harrow. Quantum supremacy through the quantum approximate optimization algorithm. *arXiv preprint arXiv:1602.07674*, 2016.
- [14] R. P. Feynman. Simulating physics with computers. *International journal of theoretical physics*, 21(6):467–488, 1982.
- [15] E. S. Fried, N. P. Sawaya, Y. Cao, I. D. Kivlichan, J. Romero, and A. Aspuru-Guzik. qTorch: The quantum tensor contraction handler. *arXiv preprint arXiv:1709.03636*, 2017.
- [16] J. M. Gambetta, J. M. Chow, and M. Steffen. Building logical qubits in a superconducting quantum computing system. *arXiv preprint arXiv:1510.04375*, 2015.
- [17] A. Gheorghiu, T. Kapourniotis, and E. Kashefi. Verification of quantum computation: An overview of existing approaches. *arXiv preprint arXiv:1709.06984*, 2017.
- [18] W. Gropp, E. Lusk, and A. Skjellum. *Using MPI: portable parallel programming with the message-passing interface*, volume 1. MIT press, 1999.
- [19] T. Häner and D. S. Steiger. 0.5 petabyte simulation of a 45-qubit quantum circuit. In *Proceedings of the International Conference for High Performance Computing, Networking, Storage and Analysis, SC ’17*, pages 33:1–33:10, New York, NY, USA, 2017. ACM.
- [20] A. W. Harrow and A. Montanaro. Quantum computational supremacy. *Nature*, 549(7671):203, 2017.
- [21] A. W. Joshi. *Matrices and tensors in physics*. New Age International, 1995.
- [22] C. L. Lawson, R. J. Hanson, D. R. Kincaid, and F. T. Krogh. Basic linear algebra subprograms for Fortran usage. *ACM Transactions on Mathematical Software (TOMS)*, 5(3):308–323, 1979.
- [23] R. Li, B. Wu, M. Ying, X. Sun, and G. Yang. Quantum supremacy circuit simulation on sunway taihulight. *arXiv preprint arXiv:1804.04797*, 2018.
- [24] N. M. Linke, D. Maslov, M. Roetteler, S. Debnath, C. Figgatt, K. A. Landsman, K. Wright, and C. Monroe. Experimental comparison of two quantum computing architectures. *Proceedings of the National Academy of Sciences*, page 201618020, 2017.

- [25] I. L. Markov and Y. Shi. Simulating quantum computation by contracting tensor networks. *SIAM Journal on Computing*, 38(3):963–981, 2008.
- [26] H. McCraw, D. Terpstra, J. Dongarra, K. Davis, and M. R. Beyond the CPU: Hardware performance counter monitoring on Blue Gene/Q. In *Proceedings of the International Supercomputing Conference 2013*, volume 7905 of *LNCS*, pages 213–225, Heidelberg, June 2013. Springer.
- [27] R. Orús. A practical introduction to tensor networks: Matrix product states and projected entangled pair states. *Annals of Physics*, 349:117–158, 2014.
- [28] C. Porter and R. Thomas. Fluctuations of nuclear reaction widths. *Physical Review*, 104(2):483, 1956.
- [29] J. Preskill. Quantum computing and the entanglement frontier. *arXiv preprint arXiv:1203.5813*, 2012.
- [30] M. Reed, L. DiCarlo, B. Johnson, L. Sun, D. Schuster, L. Frunzio, and R. Schoelkopf. High-fidelity readout in circuit quantum electrodynamics using the jaynes-cummings nonlinearity. *Physical review letters*, 105(17):173601, 2010.
- [31] M. B. Şahinoğlu, D. Williamson, N. Bultinck, M. Mariën, J. Haegeman, N. Schuch, and F. Verstraete. Characterizing topological order with matrix product operators. *arXiv preprint arXiv:1409.2150*, 2014.
- [32] E. Solomonik, D. Matthews, J. R. Hammond, J. F. Stanton, and J. Demmel. A massively parallel tensor contraction framework for coupled-cluster computations. *Journal of Parallel and Distributed Computing*, 74(12):3176–3190, 2014.
- [33] I. B. G. team. Design of the IBM Blue Gene/Q compute chip. *IBM Journal of Research and Development*, 57(1/2):1:1–1:13, Jan 2013.